WEDGE: imputation of gene expression values from single-cell RNA-seq datasets using biased matrix decomposition

Yinlei Hu[1,2,5], Bin Li[1,5], Wen Zhang[1], Nianping Liu[1], Pengfei Cai[1], Falai Chen[2,*], Kun Qu[1,3,4,*]

[1]Department of Oncology, The First Affiliated Hospital of USTC, Division of Molecular Medicine, Hefei National Laboratory for Physical Sciences at Microscale, School of Basic Medical Sciences, Division of Life Sciences and Medicine, University of Science and Technology of China, 230021 Hefei, Anhui, China.

[2]Department of Mathematics, University of Science and Technology of China

[3]CAS Center for Excellence in Molecular Cell Sciences, the CAS Key Laboratory of Innate Immunity and Chronic Disease, University of Science and Technology of China, 230027 Hefei, Anhui, China.

[4]School of Data Science, University of Science and Technology of China, 230026 Hefei, China.

[5]These authors contributed equally: Yinlei Hu, Bin Li.

*Corresponding authors: Kun Qu (qukun@ustc.edu.cn), Falai Chen (chenfl@ustc.edu.cn)

Running title: WEDGE: imputation of gene expression values

Keywords: Single-cell RNA-seq, Imputation, Denoising, Matrix decomposition

ABSTRACT

The low capture rate of expressed RNAs from single-cell sequencing technology is one of the major obstacles to downstream functional genomics analyses. Recently, a number of imputation methods have emerged for single-cell transcriptome data, however, recovering missing values in very sparse expression matrices remains a substantial challenge. Here, we propose a new algorithm, WEDGE (WEighted Decomposition of Gene Expression), to impute gene expression matrices by using a biased low-rank matrix decomposition method (bLRMD). WEDGE successfully recovered expression matrices, reproduced the cell-wise and gene-wise correlations, and improved the clustering of cells, performing impressively for applications with multiple cell type datasets with high dropout rates. Overall, this study demonstrates a potent approach for imputing sparse expression matrix data, and our WEDGE algorithm should help many researchers to more profitably explore the biological meanings embedded in their scRNA-seq datasets.

INTRODUCTION

Single-cell sequencing technology has been widely used in studies of many biological systems, including but not limited to embryonic development (Xue et al. 2013; Yan et al. 2013; Klein et al. 2015), neuronal diversity (Zeisel et al. 2015; Lake et al. 2016; Lake et al. 2018) and a large variety of diseases (Zheng et al. 2017; Guo et al. 2018; Zhang et al. 2018; Peng et al. 2019a; Zhang et al. 2019). Despite the rapid increase in sequencing throughput, the number of captured genes per cell is still limited by

technical challenges (Grün et al. 2014; Stegle et al. 2015; Kiselev et al. 2019; Hou et al. 2020). The dropout events in single-cell sequencing experiments lead to sparse expression matrices, which hinders subsequent studies (Kiselev et al. 2019; Tian et al. 2019). To overcome this, a variety of algorithms have been developed to impute the zero elements in the expression matrices (Chen and Zhou 2018; Huang et al. 2018; Linderman et al. 2018; van Dijk et al. 2018; Eraslan et al. 2019; Peng et al. 2019b; Wagner et al. 2019; Wang et al. 2019; Elyanow et al. 2020).

For example, MAGIC (van Dijk et al. 2018) recovers gene expression by using data diffusion to construct an affinity matrix which attempts to represent the neighborhood of similar cells. Huang *et al*. combined Bayesian and Poisson LASSO regression methods into SAVER (Huang et al. 2018) to estimate prior parameters and to restore missing elements of an expression data matrix, based on the assumption that gene expression follows the negative binomial distribution. Recently, they upgraded this approach to SAVER-X (Wang et al. 2019) by training a deep autoencoder model with gene expression patterns obtained from public single-cell data repositories. Eraslan *et al*. developed a deep neuron network model, DCA (Eraslan et al. 2019), which can denoise scRNA-seq data by learning gene-specific parameters. Many other tools have also emerged recently, such as SCRABBLE (Peng et al. 2019b), VIPER (Chen and Zhou 2018), ENHANCE (Wagner et al. 2019), ALRA (Linderman et al. 2018), and netNMF-sc (Elyanow et al. 2020), each of which seeks to improve recovery of the expression matrix for single-cell data. However, for datasets with high dropout rates—which therefore have very sparse expression matrices—it is still a challenge to

abundantly recover gene expression data while avoiding over-imputing (Tian et al. 2019; Elyanow et al. 2020).

Here, we introduce a new algorithm, WEDGE, to impute gene expression values for sparse single-cell data based on low-rank matrix decomposition (Kim and Park 2008; Kim and Choi 2009; Wang et al. 2015). We applied WEDGE to multiple scRNA-seq datasets and compared its performance against several state-of-the-art methods. We also examined WEDGE's ability to distinguish cell subpopulations in the Tabula Muris dataset (Tabula Muris et al. 2018), and assessed its performance for accurately imputing marker gene expression in a recently released dataset for peripheral blood mononuclear cells (PBMCs) from COVID-19 patients (Guo et al. 2020). Finally, we assessed the computer resources WEDGE consumes when analyzing large datasets.

RESULTS

Algorithm, performance, and robustness of WEDGE

The expression matrices obtained from single-cell sequencing experiments are sparse, caused by the low RNA capture rates during experimental sampling and processing (Chen and Zhou 2018; Eraslan et al. 2019). Weighted non-negative matrix factorization (WNMF) has demonstrated its potential for recovering missing elements from a sparse matrix (Kim and Choi 2009; Elyanow et al. 2020). However, it should be noted that the contribution of the zero elements in the raw matrix is completely ignored in the WNMF optimization process. In WEDGE, we adopted a low weight ($0 \leq \lambda \leq 1$) for the zero

elements in the raw expression matrix during the low-rank decomposition (a so-called bLRMD method), and generated a convergent imputed matrix using an alternating non-negative least-squares algorithm (Fig. 1A and Methods). We chose not to set λ as zero, as the contribution of the zero elements is not completely negligible (Eraslan et al. 2019). Notably, as WEDGE is a completely unsupervised algorithm, it allows us to impute expression data matrices without any prior information about genes or cell types.

To test the performance of WEDGE in restoring gene expression, we first applied it to assess a simulated dataset generated using Splatter (Zappia et al. 2017) and compared WEDGE against DCA (Eraslan et al. 2019), MAGIC (van Dijk et al. 2018), and SAVER-X (Wang et al. 2019) (Fig. 1B). The reference data includes distinct marker genes for 6 different cell types and a dense expression matrix (original sparsity=10%, where sparsity is the percentage of zero elements). Based on the assumption that gene expression values follow a negative binomial distribution (Zappia et al. 2017), the Splatter simulation set 45% of the elements in the reference data to zero (*i.e.*, dropout rate=0.45) to simulate dropout events and to obtain a down-sampled matrix, which we refer to as the “observed” data. The dropout events obscured the significance of the differentially expressed (DE) genes, but WEDGE successfully recovered their expression patterns, obtaining an imputed matrix apparently similar to the reference matrix, especially for the DE genes in cell type 1.

Also, we adopted the tSNE algorithm to explore the intercellular relationships in two-dimensional space, and used the adjusted random index (ARI) (Kiselev et al. 2017;

Huang et al. 2018) to assess the accuracy of the cell clustering results (Fig. 1C), wherein a higher ARI value indicates that the clustering result is relatively closer to the "true" cell types. Using the expression matrix imputed by WEDGE, we can clearly distinguish these cell types. The ARI value of the cell clusters from the WEDGE imputed matrix is 0.99, higher than those from the other three imputation methods.

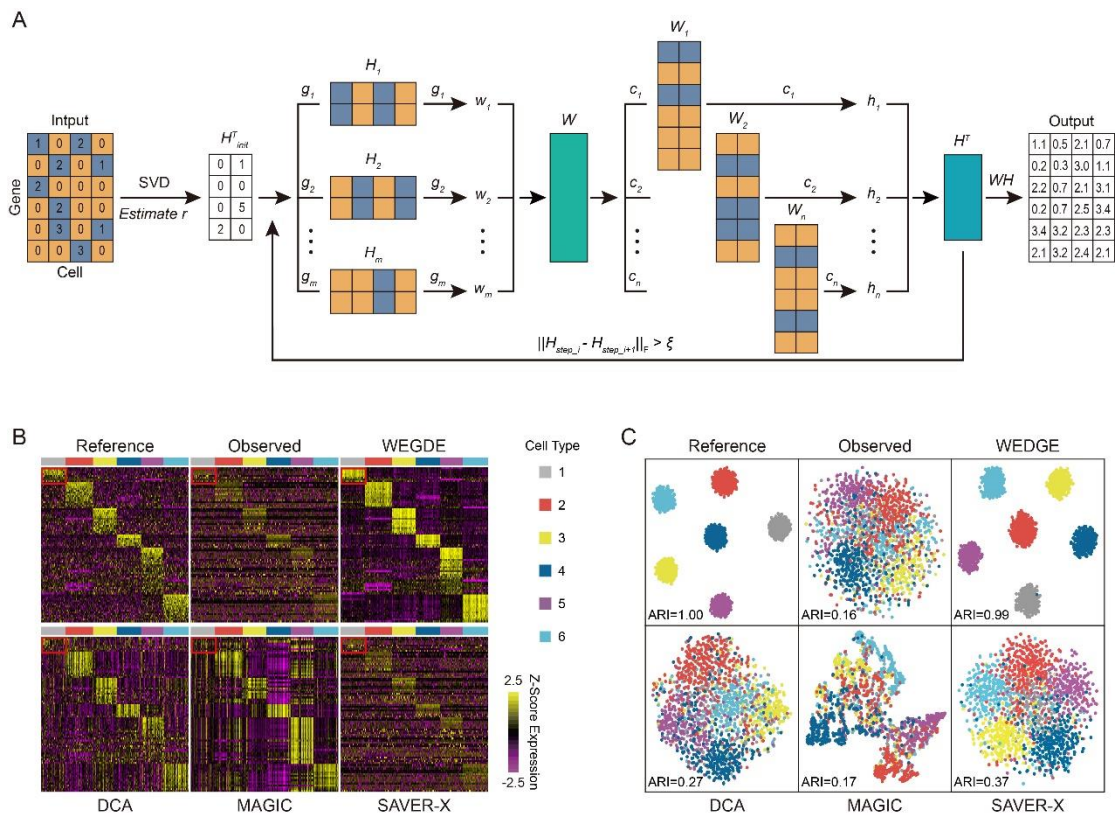

Figure 1. Design of the WEDGE algorithm and its performance for the simulated dataset. (**A**) Conceptual overview of the WEDGE workflow, where $\boldsymbol{H}$ and $\boldsymbol{W}$ are the low-dimensional representations of cells and genes respectively, $\boldsymbol{g}_i$ is the *i*th gene, $\boldsymbol{c}_j$ is the *j*th cell, $\boldsymbol{w}_i$ is the *i*th row of $\boldsymbol{W}$, and $\boldsymbol{h}_j$ is the *j*th column of $\boldsymbol{H}$. The yellow elements in $\boldsymbol{H}_i$ and $\boldsymbol{W}_j$ correspond to the zero elements in column *i* and row *j* of the original expression matrix, respectively, while the steel-blue elements represent the non-zero elements. ξ is the convergence criterion (=1×10^{-5} by default). (**B**) Expression matrices of the top DE genes of the simulated reference and observed data (with dropout rate=0.45), and the results generated by WEDGE, DCA, MAGIC, and SAVER-X. The color bar at the top indicates different cell types. (**C**) tSNE (t-distributed Stochastic Neighbor Embedding) maps of the cells from the expression matrices imputed by different methods.

125 We further evaluated the robustness of WEDGE by applying it to impute "observed"
126 matrices with different dropout rates (Supplemental Fig. S1). Interestingly, for the
127 observed matrix with a low dropout rate (0.15), all the four methods (WEDGE, DCA,
128 MAGIC, and SAVER-X) successfully recovered the distinctions between the cell types.
129 However, for the data with higher sparsity (*i.e.*, dropout rate>0.45) only WEDGE can
130 still delineate the cell identities, demonstrating the advantage of WEDGE on imputing
131 scRNA profiles with low capture rate.

132 In addition, to check whether the algorithm leads to over-imputing—for example,
133 erroneously restoring non-DE genes so that they appear as DE genes—we applied
134 WEDGE on another Splatter simulated dataset comprising 2 cell types (each with 1000
135 cells), 38 DE genes, and 162 non-DE genes. The sparsity of the reference and
136 "observed" datasets were 7% and 40%, respectively. We clustered the cells using the
137 DE gene expression values imputed by WEDGE, and the ARI value obtained was
138 equal to 0.99, which was higher than other methods. (Supplemental Fig. S2A). In
139 contrast, it was not possible to distinguish cell types based on the non-DE genes after
140 WEDGE imputation (Supplemental Fig. S2B), implying that WEDGE is robust to over-
141 imputing.

142

143 **Recovery performance for real scRNA-seq datasets**

144 To examine the performance of WEDGE on real scRNA-seq data, we applied it to
145 Zeisel's dataset (Zeisel et al. 2015) on mouse brain scRNA-seq. We first constructed

146 the reference matrix by extracting all the cells with more than 10000 UMI counts and
147 all the genes detected in more than 40% of cells, and then generated an "observed"
148 matrix with high sparsity by randomly setting a large proportion of the non-zero
149 elements to zeros (dropout rate=0.85). From the heatmaps of gene expression
150 matrices (Fig. 2A), we can see that WEDGE recovered the expression of the DE genes,
151 especially those differentially expressed between interneurons and S1 pyramidal cells.

152 We also used other tools, including SCRABBLE (Peng et al. 2019b), VIPER (Chen and
153 Zhou 2018), ENHANCE (Wagner et al. 2019), ALRA (Linderman et al. 2018), and
154 netNMF-sc (Elyanow et al. 2020) to assess the same "observed" matrix (Supplemental
155 Fig. S3A). To quantify the similarity between the reference and imputed expression
156 matrices, we calculated the cell-wise and gene-wise Pearson correlations between
157 them (Huang et al. 2018), where higher correlation coefficients indicate better recovery
158 performance. For cell-wise correlation coefficients, the WEDGE result (median
159 value=0.81) is the highest among all the tested methods (Fig. 2B). The gene-wise
160 correlation coefficients from WEDGE was also higher than that from the rest of the
161 methods. Moreover, we computed the correlation matrix distances (CMDs) (Herdin et
162 al. 2005; Huang et al. 2018) between the reference and imputed data, where a lower
163 CMD indicates that the imputed data is closer to the reference data (Fig. 2C). For the
164 matrix generated by WEDGE, the cell-to-cell CMD is 0.03 and the gene-to-gene CMD
165 is 0.12, which are each tied for the lowest of all the tested methods. These comparisons
166 together highlight that our WEDGE approach can recover both the cell-cell and gene-
167 gene correlations from sparse single-cell RNA-seq datasets.

168 In the tSNE map of cells, WEDGE can clearly distinguish interneurons, S1 pyramidal
169 neurons, and CA1 pyramidal neurons, and the ARI value of 0.56 for the clustering
170 result calculated from its imputed matrix is the highest among all tested methods (Fig.
171 2D; Supplemental Fig. S3B). In particular, in visualizing the expression of an
172 interneuron marker gene *Gad1* (Zeisel et al. 2015) and an S1 pyramidal marker gene
173 *Tbr1*, WEDGE appropriately recovered their expression levels in the corresponding
174 cell types, without overestimating their expression in other cell types (Fig. 2E;
175 Supplemental Fig. S3C). Furthermore, we also applied WEDGE to Zeisel's raw dataset
176 (Zeisel et al. 2015), which includes 3005 cells and 19973 genes. After processing with
177 WEDGE, the clustering performance index ARI increased from 0.42 (raw data) to 0.56,
178 the highest among all tested methods (Supplemental Fig. S4).
179

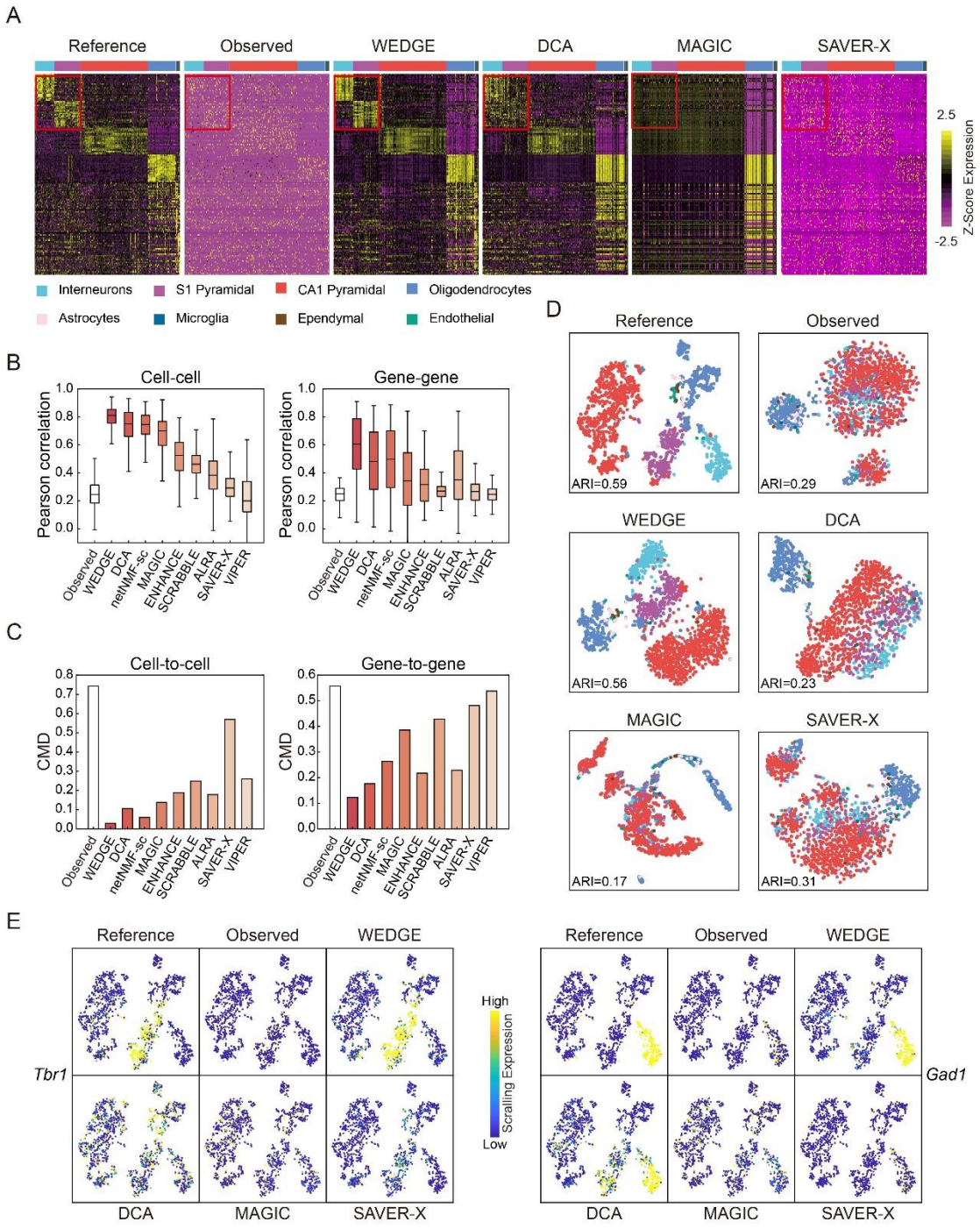

Figure 2. Application and performance assessment of WEDGE for Zeisel's single-cell sequencing dataset, compared to existing methods. (**A**) Visualizations of the expression matrices of the top DE genes of different cell types, including the reference data, the observed data (dropout rate=0.85), and the imputed data generated by four different methods. The color bar at the top indicates known cell types. (**B**) Pearson correlation coefficients between the reference and imputed matrices for cells (left panel) and genes (right panel). Center line, median; box limits, upper and lower quartiles; whiskers, 1.5x interquartile range. (**C**) Distances of the cell-to-cell (left panel) and gene-to-gene (right panel) correlation matrices between the reference and imputed data. (**D**) 2-D tSNE maps of the cells from the reference, observed, and imputed datasets. The color scheme is the

191 same as in (A). (**E**) Expression of the *Tba1* gene (left panel, a marker of S1 Pyramidal cells)
192 and the *Gad1* gene (right panel, a marker of interneurons) as imputed by different methods,
193 rendered in tSNE space.

194

195 As another example to confirm the utility of WEDGE, we applied the same procedures
196 described above to Baron's pancreas single-cell dataset (Baron et al. 2016), and
197 compared WEDGE with other imputation methods. WEDGE recovered the expression
198 of most of the DE genes, especially those of the ductal and activated stellate cells
199 (Supplemental Fig. S5A). Similarly, the cell-wise and gene-wise Pearson correlation
200 coefficients from WEDGE are both greater than those from any other tested methods,
201 emphasizing its strong recovery performance (Supplemental Fig. S5B). Moreover,
202 WEDGE's cell-to-cell and gene-to-gene CMDs of, respectively, 0.02 and 0.11 were
203 each the lowest for any of the tested methods (Supplemental Fig. S5C). Finally, in
204 terms of cell clustering, WEDGE clearly classified alpha, beta, delta, ductal, acinar,
205 and gamma cells, with an ARI value of 0.80, higher than those from all the other
206 methods (Supplemental Fig. S5D).

207

208 **Classification of cell subpopulations**

209 To test that if WEDGE can be applied for large datasets with multiple tissues and
210 organs, we used it to process the recently released Tabula Muris dataset of mouse
211 (10X Chromium sequencing data) (Tabula Muris et al. 2018). We used the k-nearest-
212 neighbor graph based method in Seurat to cluster cells for both the raw and imputed
213 data, and presented the results in tSNE space (Supplemental Fig. S6A&B). Among the

214 54 cell clusters generated from the raw data, 45 clusters have Jaccard index values
215 greater than 0.5, indicating that they were also identified in the clustering of the
216 WEDGE imputed data. (Supplemental Fig. S6C; see Methods). Notably, the WEDGE
217 imputation improved the clustering resolution for some cell types: a main cluster of B
218 cells (Supplemental Fig. S7) was classified into 4 sub-clusters (clusters 1, 3, 50, and
219 53; Fig. 3A), whereas these sub-clusters were not separated based on the raw data
220 (Fig. 3B). Most cells in clusters 1, 3, 53 are from the spleen, while cluster 50 is
221 dominated by B cells from lungs (Fig. 3C).

222 Cluster 3 splenic B cells strongly expressed the marginal zone B cell (MZ) marker *Cr2*
223 (Martin and Kearney 2002), whereas cluster 1 splenic B cells were characterized by
224 strong expression of the follicular B cell (FO) marker *Fcer2a* (Martin and Kearney 2002)
225 (Fig. 3D&E). We developed a factor called "expression bias" (see Methods for the
226 formula) to assess how a given imputation method affects the differential enrichment
227 trend for inter-cluster expression comparisons. WEDGE imputation increased the
228 expression bias of *Cr2* in cluster 3 from 0.74 to 0.88, and increased the expression
229 bias of *Fcer2a* in cluster 1 from 0.56 to 0.96. The marker gene sets characteristic of
230 MZ and FO splenic B cell subsets as reported by Kleiman (Kleiman et al. 2015) were
231 also differentially expressed in cluster 3 and 1 respectively, and WEDGE respectively
232 amplified the expression bias of these marker gene sets from 0.59/0.60 to 0.97/0.89
233 (Fig. 3F&G). Moreover, we tested the expression of the marker gene sets of the two
234 cell types reported by Newman *et al*. (Newman et al. 2017), which also supported our
235 classification of these two respective cell subpopulations as MZ and FO splenic B cells

(Supplemental Fig. S8A&B). We noted that neither the raw data nor the WEDGE imputed data showed any obvious expression of the transitional B cell marker *Cd93* (Martin and Kearney 2002) (Supplemental Fig. S8C), and it was also notable that cluster 53 apparently represented an aggregation of cells with detected transcripts for fewer than 600 genes (Supplemental Fig. S8D).

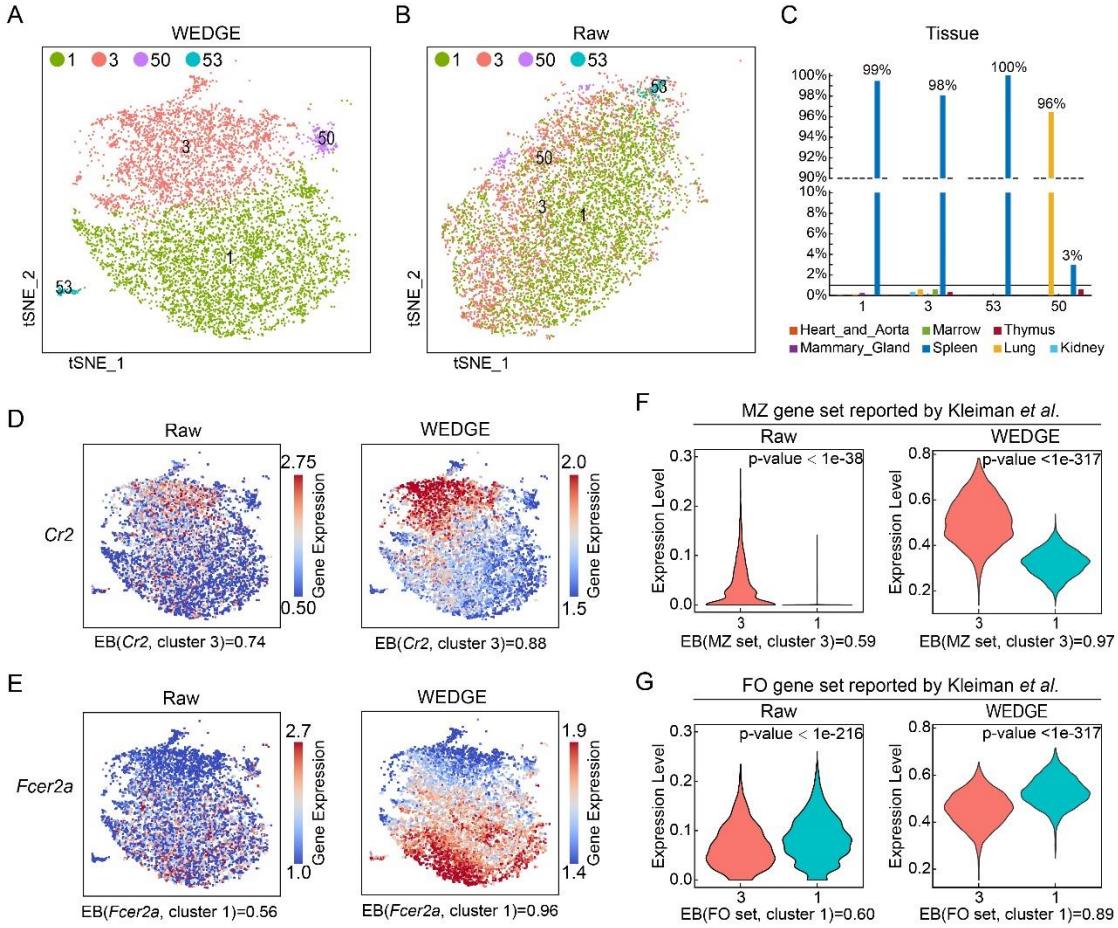

Figure 3. WEDGE imputation of the Tabula Muris dataset facilitated the classification of splenic B cell subpopulations. (**A, B**) 2-D tSNE maps of the splenic B cells generated from the WEDGE imputed data (A) and the raw data (B). The colors indicate cell clusters from the WEDGE imputed data. (**C**) The ratio of cells from different organs in splenic B cell clusters. (**D, E**) The expression of *Cr2* (D) or *Fcer2a* (E) in the raw and WEDGE imputed data, rendered in the 2-D tSNE space. EB: expression bias (see Methods). (**F, G**) The average expression of the marker gene sets of MZ (F) and FO (G) cells (reported by Kleiman *et al*. (Kleiman et al. 2015)) from the raw and WEDGE imputed data.

We also used other state-of-the-art methods to impute the same dataset and checked their clustering results on the splenic B cells (Supplemental Fig. S9). DCA, MAGIC, ALRA, and ENHANCE enhanced the expression of *Cr2* and *Fcer2a* in some cells, but these methods also amplified batch effects, and clustering based on the imputation data from these methods did not clearly distinguish splenic B cells into FO and MZ subpopulations. SAVER-X did not classify the FO and MZ subpopulations based on differential expression trends for *Cr2* or *Fcer2a*. In addition, VIPER and SCRABBLE were unable to obtain imputation results from this dataset within 100 hours on the computer with 72 CPU-cores (2.2GHz) and 1TB memory, and netNMF-sc did not complete because of memory errors.

Imputation of gene expression for the COVID-19 dataset

In a previous study of COVID-19 patients, Guo *et al.* (Guo et al. 2020) reported that one monocyte subset was found to strongly impact cytokine storms in patients classified as severe-stage. Cells of this severe-stage-specific monocyte subset strongly express many cytokines and related transcription factors such as *IL6*, *IL10*, *CXCL2*, *CXCL3*, *CCL4*, *ATF3*, *TNF*, and *HIVEP2*. However, dropout events in single cell sequencing experiments obscured this trend. Here, we applied WEDGE to this recently released COVID-19 dataset containing 13239 PBMCs from patients and 54951 PBMCs from healthy donors (Guo et al. 2020). The clusters obtained from the WEDGE imputed data correspond to cell clusters reported in the original paper (Guo et al. 2020), with an ARI value of 0.70, the highest among all tested methods (Fig.

4A&B). Guo *et al.* divided the monocyte cells into clusters 2, 9, 13, and 16, with the cells in cluster 9 apparently representing the severe-stage-specific monocyte subset (Guo et al. 2020). Following WEDGE imputation, the severe-stage-specific cytokines and upstream transcription factors reported by Guo *et al.* had increased expression bias in cluster 9 cells (from 0.03~0.93 to 1.00; Fig. 4D). Notably, the DE genes of cluster 9 generated from the WEDGE imputed data cover 99% of the DE genes in the raw data (Fig. 4C). The WEDGE imputed data also increased the expression bias of the *APOE* and *CXCR3* genes in cluster 9 cells (Supplemental Fig. S10A). Similar increases in expression bias were detected in the WEDGE imputed data for severe-stage-specific DE genes reported by Wilk *et al.* (Wilk et al. 2020) (Supplemental Fig. S10B).

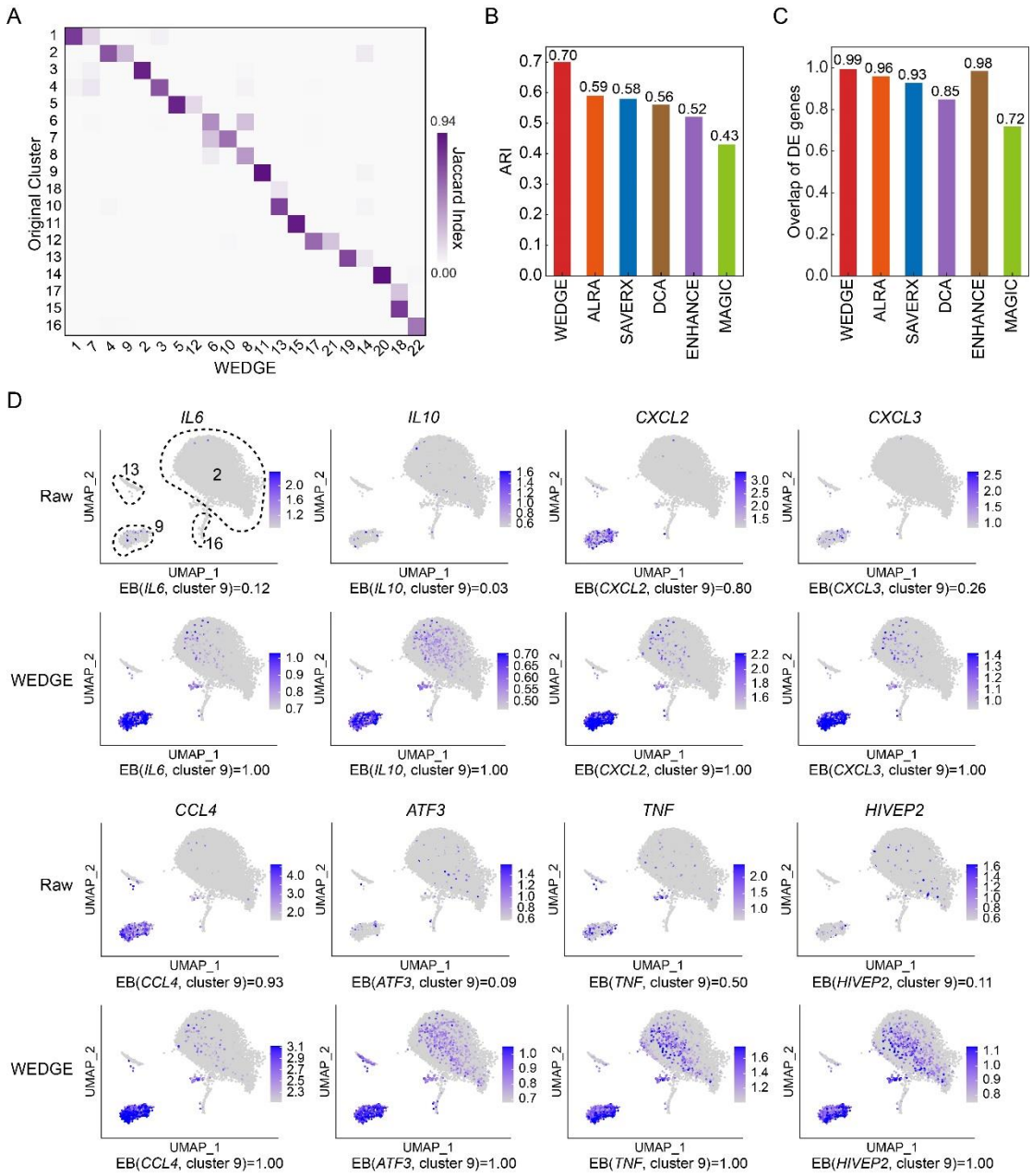

Figure 4. WEDGE enhanced marker gene expression for COVID-19 data from Guo *et al.* (**A**) Jaccard index between the cell clusters reported by Guo *et al.* (2020) and the clusters generated from WEDGE imputed data. (**B**) ARI values calculated from the clustering results of the imputed data generated by different methods. The results of other methods are not shown, as SCRABBLE did not finish the imputation within 100 hours on a computer with 72 CPU-cores (2.2GHz) and 1TB memory, and both VIPER and netNMF-sc reported memory errors. (**C**) Proportion of the reported DE genes that can be regenerated from the imputed data, *i.e.*, $\frac{|D_{raw} \cap D_{imputed}|}{|D_{raw}|}$, here, D_{raw} and $D_{imputed}$ are DE gene sets generated from the raw data and the imputed data, respectively. (**D**) The expression of known marker genes of severe-stage specific monocytes. Clusters 2, 9, 13, and 16 are cell clusters reported by the original paper. EB: expression bias (see Methods).

296 **Scalability and efficiency**

297 To quantify the scalability and efficiency of different imputation algorithms, we counted
298 the time and memory consumption of WEDGE and other state-of-the-art methods
299 when imputing Tabula Muris dataset that contains 55656 cells and 23341 genes (after
300 filtering). WEDGE consumed 1 hour and up to 38GB of memory on a 72-core computer
301 to complete the imputation process, which was close to the MAGIC method. (Fig.
302 5A&B). To further assess the computer resources that WEDGE spends on datasets of
303 various sizes, we applied it to impute datasets comprising different numbers of cells
304 (5000~1000000) but a fixed number of genes (2000), which were sampled from the
305 mouse brain atlas project (see Methods). The runtime of WEDGE increased linearly
306 with the number of cells, and its speed was close to DCA and MAGIC (Fig. 5C). For
307 the dataset containing 1 million cells and 2000 genes, WEDGE finished the imputation
308 of missing values in 12 minutes. Notably, WEDGE offers a visual interactive interface,
309 making it convenient for researchers to use. We have uploaded WEDGE and the
310 datasets used in this study to GitHub (https://github.com/QuKunLab/WEDGE).

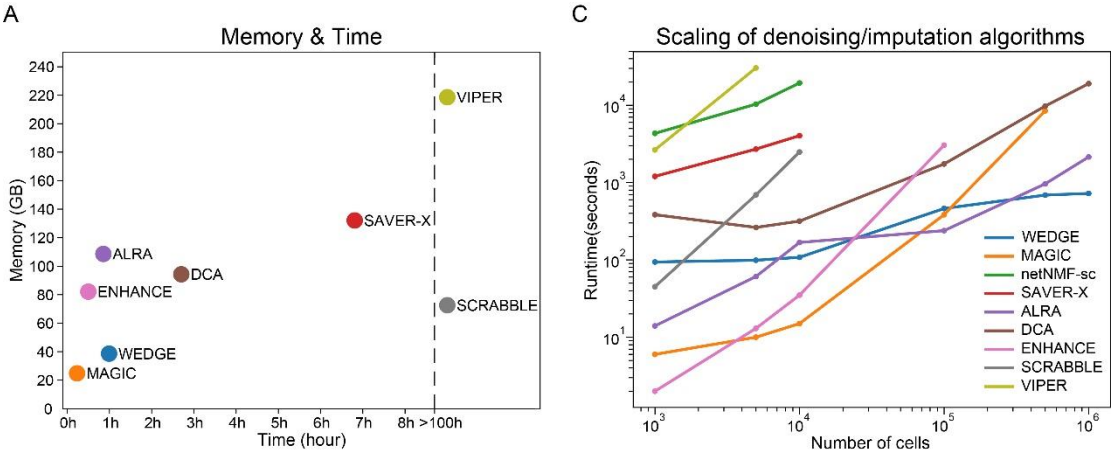

B

Runtime & Memory requirement of imputation methods on Tabula Muris dataset

Methods	WEDGE	DCA	MAGIC	SAVER-X	ALRA	ENHANCE	VIPER	SCRABBLE	netNMF-sc
Memory (GB)	38.6G	94.3G	24.8G	132.1G	108.6G	82.1G	218.6G	72.6G	NA
Time(s)	3567s	9710s	836s	24508s	3081s	1793s	>100h	>100h	NA

Figure 5. Computer resources consumed by different imputation methods, on a computer with 72 CPU-cores and 1TB memory. (**A, B**) The runtime and memory spent by different methods for imputing the Tabula Muris dataset, where netNMF-sc reported errors and stopped running. (**C**) The computational cost of different methods for imputing single-cell datasets of various sizes. Results that took more than 9 hours or reported memory errors are not shown here.

DISCUSSION

Here, we present an approach, WEDGE, to impute missing gene expression information in single-cell sequencing datasets that is based on the combination of low-rank matrix decomposition and biased weight parameters for the zero and non-zero elements in the expression matrix. We demonstrate that the usage of WEDGE significantly improves the clustering accuracy of many scRNA-seq datasets, amplifies the contribution of differential genes to identifying cell types, and helps distinguish more cell subpopulations from low-quality data.

We tested the impact of the bias parameter λ on imputation, which indicated that recovery performance is insensitive to λ for datasets with dropout rates less than 0.6 (Supplemental Fig. S11; see Methods). For the datasets with dropout rates greater than 0.6, λ values between 0.1~0.15 can produce the best recovery results. We thus set $\lambda = 0.15$ for all datasets presented in this paper. The imputation contribution of the zero elements decreases with the increase of matrix sparsity, but it cannot be ignored, which implies that some zero elements may be related to the low expression of certain genes, rather than simply reflecting experimental noise.

There are still challenges for the informative imputation of scRNA-seq datasets, such as how to recover the heterogeneity between cell types instead of experimental batches, how to discover cell subtypes with very few cells from the imputed data, and how to use limited computer resources to process large datasets containing millions of cells. Moreover, it necessary to assess whether current imputation methods are applicable to datasets obtained using diverse bioanalytical methods beyond standard RNA-seq (e.g., single-cell ATAC-seq and profiling methods for various epigenomic modifications).

METHODS

Imputation model of WEDGE

WEDGE takes an expression matrix $\boldsymbol{A}_{m\times n}$ as input, where the element $\boldsymbol{a}_{ij}$ represents the expression of the ith gene in the jth cell. By default, it normalizes the

348 total expression of each cell to 10,000, and updates the expression value by
349 performing a logarithm on it, *i.e.*, $\boldsymbol{a_{ij}} = \log\left(\frac{\boldsymbol{a_{ij}} \times 10000}{\sum_i \boldsymbol{a_{ij}}} + 1\right)$. After imputation, WEDGE
350 outputs two non-negative matrices, $\boldsymbol{W}$ and $\boldsymbol{H}$; we can then take their matrix product
351 as the final imputed expression matrix, $\boldsymbol{V}$. In the WEDGE algorithm, we imputed
352 single-cell sequencing data through the following optimization framework:

353
$$\begin{aligned} &Obj = \min_{W,H} \sum_{i,j\in\Omega} \left|\boldsymbol{a}_{ij} - \boldsymbol{v}_{ij}\right|^2 + \lambda \sum_{ij\in\bar{\Omega}} \left|\boldsymbol{v}_{ij}\right|^2 \\ &\text{subject to } \boldsymbol{v}_{ij} = \sum_{k=1}^{r} \boldsymbol{w}_{ik}\boldsymbol{h}_{kj}, \boldsymbol{H} \in \mathbb{R}^{+}_{r\times n}, \boldsymbol{W} \in \mathbb{R}^{+}_{m\times r}, \end{aligned} \tag{1}$$

354 where $\boldsymbol{\Omega} = \{(i,j)|\boldsymbol{a}_{ij} > 0, i = 1\sim m, j = 1\sim n\}$, $\bar{\boldsymbol{\Omega}}$ is the complementary set of $\boldsymbol{\Omega}$ when
355 the universe is $\{(i,j)|i = 1\sim m, j = 1\sim n\}$, $\boldsymbol{v}_{ij}$ is the element of the ith row and jth
356 column of $\boldsymbol{V}$, $\boldsymbol{w}_{ik}$ represents the element of matrix $\boldsymbol{W}$, and $\boldsymbol{h}_{kj}$ is the element of
357 matrix $\boldsymbol{H}$. In this model, the first term in the objective function guarantees minimization
358 of approximation error between the non-zero elements of the original matrix $\boldsymbol{A}$ and
359 the corresponding elements in the imputed matrix $\boldsymbol{V}$, while the second term tends to
360 minimize the elements in $\boldsymbol{V}$ which correspond to zero elements in $\boldsymbol{A}$. The non-
361 negative constraints in model (1) ensure that all the entries of $\boldsymbol{V}$ are no-negative.

362 Users can tune $\lambda \in [0,1]$ to balance the contributions of the two terms of the objective
363 functions. In order to study the influence of λ on the recovery performance, we down-
364 sampled the reference data of the Zeisel and Baron datasets and adopted different
365 dropout rates. By computing the correlation matrix distances (CMDs) (Herdin et al.
366 2005; Huang et al. 2018) between the reference data and the imputed data, we found
367 that the recovery performance is not sensitive to the change of λ when the dropout
368 rate is less than 0.6. For data with drop rate greater than 0.6, the best imputation result

can be obtained by setting λ to 0.1~0.15. We set $\lambda = 0.15$ for all the datasets used in this study, which is also the default value for WEDGE.

Optimization of the model

In the WEDGE algorithm, the matrix $\boldsymbol{W}$ and $\boldsymbol{H}$ were separately considered, which means that we fixed $\boldsymbol{H}$ to optimize $\boldsymbol{W}$, and then fixed $\boldsymbol{W}$ to generate the new $\boldsymbol{H}$. First, we defined that $\boldsymbol{g}_i$ is the ith row of $\boldsymbol{A}$, $\boldsymbol{H}_i^+$ and $\boldsymbol{H}_i^0$ are composed of the $\boldsymbol{H}$ columns that correspond to the non-zero and zero elements of $\boldsymbol{g}_i$ respectively, and $\boldsymbol{g}_i^+$ is the vector after deleting all zero elements from $\boldsymbol{g}_{\mathrm{i}}$. Then we rewrote the objective function of solving $\boldsymbol{W}$, as,

$$\min_{\boldsymbol{w}_i} \|\boldsymbol{w}_i \boldsymbol{H}_i^+ - \boldsymbol{g}_i^+\|_2^2 + \lambda \left\|\boldsymbol{w}_i \boldsymbol{H}_i^0\right\|_2^2 = \min_{\boldsymbol{w}_i} \left\|\boldsymbol{w}_i \widetilde{\boldsymbol{H}}_i - \boldsymbol{g}_i\right\|_2^2 \tag{2}$$

where $\widetilde{\boldsymbol{H}}_i$ is the combination of $\boldsymbol{H}_i^+$ and $\lambda \boldsymbol{H}_i^0$ according to the original order of their elements in $\boldsymbol{H}$, and $\boldsymbol{w}_i$ is the ith row of $\boldsymbol{W}$. In this case, optimizing $\boldsymbol{W}$ is equivalent to solving m non-negative least-squares problems (2) in parallel (Lawson and Hanson 1995). After $\boldsymbol{W}$ was obtained, we fixed it and solved $\boldsymbol{H}$ using similar algorithm as described above.

Algorithm 1. Optimization of WEDGE

Step1: generate the initial $\boldsymbol{H} \in \mathbb{R}^{+}_{r\times n}$ from singular value decomposition.

Step2: from a given $\boldsymbol{H}$, solve $\boldsymbol{W}$ in parallel with a non-negative least-square method.

Step3: from the $\boldsymbol{W}$ obtained in step 2, calculate a new $\boldsymbol{H}$.

Step4: iteratively return back to step 2 and 3 until the relative difference in the object function between two adjacent loops is less than 1×10^{-5} or the maximum specified number of iterations is reached.

Estimating the rank of the expression matrix

During the optimization process for WEDGE, we designed a heuristic algorithm to determine the rank of $\boldsymbol{A}_{m\times n}$ based on the relative variation of its singular values $\{\sigma_i: i = 1\sim\min(m,n)\}$. For a descending list of λ_i, we defined a function $f(\sigma_i)$ as

$$f(\sigma_i) = \begin{cases} 0, & if \ \frac{\sigma_i-\sigma_{i+1}}{\sigma_{i+1}} \geq \varepsilon \ and \ \frac{\sigma_{i+p}-\sigma_{i+p+1}}{\sigma_{i+p+1}} < \varepsilon \ for \ p \in [1,10], \\ 1, & otherwise, \end{cases} \tag{3}$$

where ε is a small non-negative constant (0.085 by default). The following provides the details of the algorithm for the evaluation of rank r:

Algorithm 2: Estimating the rank of the expression matrix

Input: the singular values of matrix $\boldsymbol{A}$: $\sigma_1 \geq \sigma_2 \geq \sigma_3 \geq \cdots \geq \sigma_{\min(m,n)}$

Output: the final rank retained for $\boldsymbol{A}$: r

Algorithm:

```
r = 1;
while f(σ_r) and r ≤ min(m,n) − 11 do
  r = r + 1;
end while
```

Correlation matrix distance (CMD)

CMD is usually used to determine the difference between two correlation matrices. It denotes the error of imputation process (Huang et al. 2018; Wang et al. 2019), as a larger CMD value indicates greater difference between the reference/raw matrix and the imputed matrix. The CMD of two correlation matrices $\boldsymbol{R}_1$, $\boldsymbol{R}_2$ is expressed as $d(\boldsymbol{R}_1,\ \boldsymbol{R}_2) = 1 - \frac{tr(\boldsymbol{R}_1\boldsymbol{R}_2)}{\|\boldsymbol{R}_1\|_f\|\boldsymbol{R}_2\|_f}$.

Jaccard index

The Jaccard index can be used to evaluate the similarity between two clusters (Levandowsky and Winter 1971). The Jaccard index of two clusters $\boldsymbol{A}$, $\boldsymbol{B}$ is defined as $r = \frac{|\boldsymbol{A}\cap\boldsymbol{B}|}{|\boldsymbol{A}\cup\boldsymbol{B}|}$, here $|\cdot|$ represented the number of elements in a set.

Expression bias

The expression bias of gene α in cell cluster C_i refers to the proportion of cells (in cluster C_i) whose expression level of gene α is higher than the average expression of other clusters:

$$EB(\alpha, C_i) = \frac{1}{N(C_i)} \sum_{k \in C_i} \delta[E(\alpha, k) - \bar{E}(\alpha, k' \notin C_i)]$$

where k is a cell belonging to cluster C_i, $E(\alpha, k)$ is the expression value of gene α in cell k, k' is a cell belonging to other clusters, $\bar{E}(\alpha, k' \notin C_i)$ is the average

417 expression value of gene α in all other clusters, $N(C_i)$ is the number of cells in cluster

418 C_i, and δ function is defined as

419 $$\delta(x) = \begin{cases} 1 & if \ \ x > 0 \\ 0 & if \ \ x \leq 0 \end{cases}$$

420

421 **Generation of the simulated scRNA-seq datasets**

422 We used the *splatSimulate()* function in the Splatter R package (Zappia et al. 2017) to

423 generate simulated datasets. For the dataset containing 6 cell types, 500 genes, and

424 2000 cells (shown in Fig. 1B-C and Supplemental Fig. S1), we set seed=42 and

425 dropout.shape=-1, and its dropout rate was tuned by parameter dropout.mid values

426 ranging from 1 to 6. For the dataset with two cell types, 200 genes, and 2000 cells

427 (shown in Supplemental Fig. S2), we set seed=42, dropout.shape=-1, and

428 dropout.mid=2.

429

430 **Processing of different datasets**

431 For Zeisel's dataset of the mouse cortex and hippocampus cells (GSE60361) (Zeisel

432 et al. 2015), we generated a reference dataset that contains high quality cells and

433 genes (performed identically with the previously described filtering step of SAVER

434 (Huang et al. 2018)), and retained all of the marker genes described in the initial Zeisel

435 study (*Tbr1*, *Spink8*, *Aldoc*, *Gad1*, *Mbp*, and *Thy1*). Then, we randomly set 85% of the

436 non-zero elements of the reference data to zeros to generate observed data with

437 dropouts. For Baron's dataset of human pancreatic islet cells (GSE84133) (Baron et

al. 2016), we also used the same process to filter the high quality cells and genes from the original data to build the reference dataset, in which 54% of the elements had non-zero values. We then randomly set 65% of the non-zero elements to zeros to simulate dropout events. For Tabula Muris dataset (GSE109774) (Tabula Muris et al. 2018), we applied the pipeline provided by Tabula Muris to filter the genes and cells, and obtained an expression matrix with 23341 genes and 55656 cells. For the COVID-19 dataset, we filtered genes and cells using the same method as Guo *et al* (Guo et al. 2020), to obtain an expression matrix containing 23,324 genes and 68,190 cells.

Parameters for other imputation tools

(1) For the application to all datasets in the paper, DCA (version 0.2.2) was performed on the expression matrices with default parameters (type = 'zinb-conddisp', hiddensize = '64,32,64' and learningrate = 0.001). (2) We ran SAVER-X (version1.0.0) on the expression matrices with default parameters. Specifically, we set “data.species = Others, use.pretrain = F” for the simulated datasets, “data.species = Mouse, use.pretrain = T, pretrained.weights.file = mouse_AdultBrain.hdf5, model.species = Mouse” for Zeisel’s dataset, and “data.species = Human, use.pretrain = T, pretrained.weights.file = human_Devbrain_nomanno.hdf5, model.species = Human” for Baron’s dataset. (3) MAGIC (Python version 1.5.5) was performed with normalized expression matrices (same as WEDGE) and default parameters (decay = 15, t = 'auto', and knn_dist = 'euclidean'). Specifically, we set the numbers of principal components to 20 and the number of nearest neighbors to 15. (4) SCABBLE (MATLAB version)

460 was performed on the library size normalized expression matrices with default
461 parameters (parameter = [1,0,1e-4], nIter = 100). (5) VIPER (version 0.1.1) was
462 performed on the expression matrices with default parameters (num = 0.8 times the
463 number of genes, percentage.cutoff = 0.1, minbool = FALSE, and alpha = 0.5). (6)
464 ALRA (RunALRA function in Seurat 3.0 (Butler et al. 2018; Stuart et al. 2019a)) was
465 performed on the expression matrices with default parameters (k = NULL, q = 10). (7)
466 ENHANCE was performed on the expression matrices with default parameters (max-
467 components = 50). (8) netNMF-sc (version 2.0) was run on the expression matrices
468 with default parameters and the outputs were used for downstream analysis.
469 Specifically, we set dimensions = 20 and normalize = False. For the matrix
470 preprocessing step of all methods, we adopted the algorithms recommended by their
471 respective tutorials. For tools that did not describe the preprocessing algorithm, we
472 used the same procedure as WEDGE.

473

474 **Parameters for cell clustering**

475 We used Scanpy (Wolf et al. 2018) (version 1.4.0) and the default parameters
476 (n_neighbors = 15 and n_pcs=50 in neighbors() function) to cluster cells for each
477 dataset. Particularly, we set the "resolution" parameter (in louvain() function) to 1 for
478 the first simulated dataset (shown in Fig. 1B-C and Supplemental Fig. S1), to 0.5 for
479 the second simulated dataset (shown in Supplemental Fig. S2), and to 0.3 for both of
480 the two real datasets (Zeisel's and Baron's datasets), to get the highest ARI value for
481 the cell clustering of each reference matrix. For the clustering of the observed and

482 imputed matrices of a given dataset, we adopted the same parameters as we used for
483 the corresponding reference matrix. We used Seurat 2.3.0 (as the original paper) with
484 parameters dims.use = 1:30 and resolution = 1.1, to cluster cells of the raw and the
485 imputed expression matrices of Tabula Muris dataset (Tabula Muris et al. 2018). For
486 the raw and imputed matrices of Guo's dataset (Guo *et al*. 2020), we used Seurat 3.2.0
487 (as the original paper) with parameters dims.use = 1:50 and resolution = 0.5 to cluster
488 cells.

489

490 **Scalability analysis**

491 Scalability analysis was performed on a super computer with four Intel Xeon E7-8860
492 v4 2.20 GHz CPUs (72 cores in total) and 1TB memory. We down-sampled the mouse
493 brain atlas dataset downloaded from 10X Genomics website
494 (https://support.10xgenomics.com/single-cell-gene-
495 expression/datasets/1.3.0/1M_neurons) to construct the benchmark datasets with
496 different number of cells (from 1000 to 1000000). First, we filtered out the genes that
497 were only expressed in three or fewer cells, and normalized the library size of the
498 dataset. Then, we used the gene filtering function of Scanpy, *i.e.*,
499 scanpy.pp.highly_variable_genes(), with min_mean=0.0125, max_mean=3,
500 min_disp=0.5 and n_top_genes=2000 to obtain the top 2000 most variable genes.
501 With the fixed number of genes, we sampled 1000, 5000, 10000, 100000, 500000, and
502 1000000 cells from the raw dataset to simulate experiments of different scales.

TSNE, UMAP, and heatmap visualization

(1) Settings for dimension reduction: For the simulated dataset, Baron's dataset, and Zeisel's datasets, we used the first 20 principal components to perform tSNE analysis. For Tabula Muris dataset (Tabula Muris et al. 2018), we performed the 2D tSNE embedding by using Seurat with parameters dims.use = 1:30, seed.use = 10, and perplexity = 30. For Guo's COVID-19 dataset, we used the same 2D UMAP method as the original paper (Guo et al. 2020). (2) Settings for heatmap: we calculated the Z-score of the expression of each gene, and used Seurat 3.0 (Butler et al. 2018; Stuart et al. 2019a; Stuart et al. 2019b) to extract the top DE genes from the reference matrix. The top 20 DE genes (only.pos = TRUE, min.pct = 0.1, and logfc.threshold = 0.25 in FindAllMarkers() function) of each cell type are shown in the heatmaps for Baron's and Zeisel's datasets (*i.e.*, Fig. 2A; Supplemental Fig. S3A & 5A), and the top 30 DE genes (only.pos = TRUE, min.pct = 0.1, and logfc.threshold = 0.15 in FindAllMarkers() function) for each cell type are shown in the heatmaps of a simulated dataset (*i.e.*, Fig. 1B). For the observed and imputed matrices of each dataset, we present the same DE genes in the same order as in the heatmap of the reference matrix.

DATA ACCESS

Published datasets used in this study: Zeisel's dataset of the mouse cortex and hippocampus cells (GSE60361), Baron's dataset of human pancreatic islet cells

(GSE84133) (Baron et al. 2016), Tabula Muris dataset including 20 mouse organs (GSE109774) (Tabula Muris et al. 2018), Guo's dataset (Guo et al. 2020) containing PBMCs from 2 COVID-19 patients (GSE150861), and the 10X dataset of 2 healthy donors (https://support.10xgenomics.com/single-cell-gene-expression/datasets/3.1.0/5k_pbmc_NGSC3_aggr). The source code of WEDGE was released at https://github.com/QuKunLab/WEDGE.

ACKNOWLEDGMENTS

This work was supported by the National Key R&D Program of China (2017YFA0102900 to K.Q.), the National Natural Science Foundation of China grants (91940306, 81788101, 31970858, 31771428 and 91640113 to K.Q.; 61972368, 11571338 to F.C.), and the Fundamental Research Funds for the Central Universities (YD2070002019 and WK2070000158 to K.Q.). We thank the USTC supercomputing center and the School of Life Science Bioinformatics Center for providing computing resources for this project.

AUTHOR CONTRIBUTIONS

K.Q. and F.C. conceived and supervised the project; Y.H. and B.L. designed implemented, and validated WEDGE with the help from W.Z., N.L. and P.C.; B.L., Y.H. and K.Q. wrote the manuscript with inputs from all the authors.

DISCLOSURE DECLARATION

The authors declare that they have no competing interests.

REFERENCES

Baron M, Veres A, Wolock SL, Faust AL, Gaujoux R, Vetere A, Ryu JH, Wagner BK, Shen-Orr SS, Klein AM et al. 2016. A Single-Cell Transcriptomic Map of the Human and Mouse Pancreas Reveals Inter- and Intra-cell Population Structure. *Cell Syst* **3**: 346-360 e344.

Butler A, Hoffman P, Smibert P, Papalexi E, Satija R. 2018. Integrating single-cell transcriptomic data across different conditions, technologies, and species. *Nature Biotechnology* **36**: 411.

Chen M, Zhou X. 2018. VIPER: variability-preserving imputation for accurate gene expression recovery in single-cell RNA sequencing studies. *Genome Biol* **19**: 196.

Elyanow R, Dumitrascu B, Engelhardt BE, Raphael BJ. 2020. netNMF-sc: leveraging gene–gene interactions for imputation and dimensionality reduction in single-cell expression analysis. *Genome research* **30**: 195-204.

Eraslan G, Simon LM, Mircea M, Mueller NS, Theis FJ. 2019. Single-cell RNA-seq denoising using a deep count autoencoder. *Nat Commun* **10**: 390.

Grün D, Kester L, Van Oudenaarden A. 2014. Validation of noise models for single-cell transcriptomics. *Nature methods* **11**: 637.

Guo C, Li B, Ma H, Wang X, Cai P, Yu Q, Zhu L, Jin L, Jiang C, Fang J. 2020. Single-cell analysis of two severe COVID-19 patients reveals a monocyte-associated and tocilizumab-responding cytokine storm. *Nature Communications* **11**: 1-11.

Guo X, Zhang Y, Zheng L, Zheng C, Song J, Zhang Q, Kang B, Liu Z, Jin L, Xing R. 2018. Global characterization of T cells in non-small-cell lung cancer by single-cell sequencing. *Nature medicine* **24**: 978.

Herdin M, Czink N, Ozcelik H, Bonek E. 2005. Correlation matrix distance, a meaningful measure for evaluation of non-stationary MIMO channels. In *2005 IEEE 61st Vehicular Technology Conference*, Vol 1, pp. 136-140. IEEE.

Hou W, Ji Z, Ji H, Hicks SC. 2020. A systematic evaluation of single-cell RNA-sequencing imputation methods. *Genome Biology* **21**: 218.

Huang M, Wang J, Torre E, Dueck H, Shaffer S, Bonasio R, Murray JI, Raj A, Li M, Zhang NR. 2018. SAVER: gene expression recovery for single-cell RNA sequencing. *Nat Methods* **15**: 539-542.

Kim H, Park H. 2008. Nonnegative matrix factorization based on alternating nonnegativity constrained least squares and active set method. *SIAM journal on matrix analysis and applications* **30**: 713-730.

Kim Y-D, Choi S. 2009. Weighted nonnegative matrix factorization. In *2009 IEEE International Conference on Acoustics, Speech and Signal Processing*, pp. 1541-1544. IEEE.

Kiselev VY, Andrews TS, Hemberg M. 2019. Challenges in unsupervised clustering of single-cell

582 RNA-seq data. *Nat Rev Genet* **20**: 273-282.
583 Kiselev VY, Kirschner K, Schaub MT, Andrews T, Yiu A, Chandra T, Natarajan KN, Reik W, Barahona
584 M, Green AR et al. 2017. SC3: consensus clustering of single-cell RNA-seq data. *Nature*
585 *Methods* **14**: 483.
586 Kleiman E, Salyakina D, De Heusch M, Hoek KL, Llanes JM, Castro I, Wright JA, Clark ES, Dykxhoorn
587 DM, Capobianco E et al. 2015. Distinct Transcriptomic Features are Associated with
588 Transitional and Mature B-Cell Populations in the Mouse Spleen. *Front Immunol* **6**: 30.
589 Klein AM, Mazutis L, Akartuna I, Tallapragada N, Veres A, Li V, Peshkin L, Weitz DA, Kirschner MW.
590 2015. Droplet barcoding for single-cell transcriptomics applied to embryonic stem cells.
591 *Cell* **161**: 1187-1201.
592 Lake BB, Ai R, Kaeser GE, Salathia NS, Yung YC, Liu R, Wildberg A, Gao D, Fung H-L, Chen S. 2016.
593 Neuronal subtypes and diversity revealed by single-nucleus RNA sequencing of the
594 human brain. *Science* **352**: 1586-1590.
595 Lake BB, Chen S, Sos BC, Fan J, Kaeser GE, Yung YC, Duong TE, Gao D, Chun J, Kharchenko PV.
596 2018. Integrative single-cell analysis of transcriptional and epigenetic states in the human
597 adult brain. *Nature biotechnology* **36**: 70-80.
598 Lawson CL, Hanson RJ. 1995. *Solving least squares problems*. Siam.
599 Levandowsky M, Winter D. 1971. Distance between Sets. *Nature* **234**: 34-35.
600 Linderman GC, Zhao J, Kluger Y. 2018. Zero-preserving imputation of scRNA-seq data using low-
601 rank approximation. *bioRxiv* doi:https://doi.org/10.1101/397588.
602 Martin F, Kearney JF. 2002. Marginal-zone B cells. *Nat Rev Immunol* **2**: 323-335.
603 Newman R, Ahlfors H, Saveliev A, Galloway A, Hodson DJ, Williams R, Besra GS, Cook CN,
604 Cunningham AF, Bell SE et al. 2017. Maintenance of the marginal-zone B cell
605 compartment specifically requires the RNA-binding protein ZFP36L1. *Nat Immunol* **18**:
606 683-693.
607 Peng J, Sun B-F, Chen C-Y, Zhou J-Y, Chen Y-S, Chen H, Liu L, Huang D, Jiang J, Cui G-S. 2019a.
608 Single-cell RNA-seq highlights intra-tumoral heterogeneity and malignant progression
609 in pancreatic ductal adenocarcinoma. *Cell research* **29**: 725-738.
610 Peng T, Zhu Q, Yin P, Tan K. 2019b. SCRABBLE: single-cell RNA-seq imputation constrained by
611 bulk RNA-seq data. *Genome Biol* **20**: 88.
612 Stegle O, Teichmann SA, Marioni JC. 2015. Computational and analytical challenges in single-cell
613 transcriptomics. *Nature Reviews Genetics* **16**: 133.
614 Stuart T, Butler A, Hoffman P, Hafemeister C, Papalexi E, Mauck III WM, Hao Y, Stoeckius M, Smibert
615 P, Satija R. 2019a. Comprehensive integration of single-cell data. *Cell* **177**: 1888-1902.
616 e1821.
617 Stuart T, Butler A, Hoffman P, Hafemeister C, Papalexi E, Mauck III WM, Hao Y, Stoeckius M, Smibert
618 P, Satija R. 2019b. Comprehensive Integration of Single-Cell Data. *Cell*.
619 Tabula Muris C, Overall c, Logistical c, Organ c, processing, Library p, sequencing, Computational
620 data a, Cell type a, Writing g et al. 2018. Single-cell transcriptomics of 20 mouse organs
621 creates a Tabula Muris. *Nature* **562**: 367-372.
622 Tian L, Dong X, Freytag S, Le Cao KA, Su S, JalalAbadi A, Amann-Zalcenstein D, Weber TS, Seidi A,
623 Jabbari JS et al. 2019. Benchmarking single cell RNA-sequencing analysis pipelines using
624 mixture control experiments. *Nat Methods* **16**: 479-487.
625 van Dijk D, Sharma R, Nainys J, Yim K, Kathail P, Carr AJ, Burdziak C, Moon KR, Chaffer CL,

Pattabiraman D et al. 2018. Recovering Gene Interactions from Single-Cell Data Using Data Diffusion. *Cell* **174**: 716-729 e727.

Wagner F, Barkley D, Yanai I. 2019. Accurate denoising of single-cell RNA-Seq data using unbiased principal component analysis. *BioRxiv* doi:https://doi.org/10.1101/655365.

Wang J, Agarwal D, Huang M, Hu G, Zhou Z, Ye C, Zhang NR. 2019. Data denoising with transfer learning in single-cell transcriptomics. *Nature Methods* **16**: 875-878.

Wang Z, Lai M-J, Lu Z, Fan W, Davulcu H, Ye J. 2015. Orthogonal rank-one matrix pursuit for low rank matrix completion. *SIAM Journal on Scientific Computing* **37**: A488-A514.

Wilk AJ, Rustagi A, Zhao NQ, Roque J, Martínez-Colón GJ, McKechnie JL, Ivison GT, Ranganath T, Vergara R, Hollis T. 2020. A single-cell atlas of the peripheral immune response in patients with severe COVID-19. *Nature Medicine*: 1-7.

Wolf FA, Angerer P, Theis FJ. 2018. SCANPY: large-scale single-cell gene expression data analysis. *Genome Biol* **19**: 15.

Xue Z, Huang K, Cai C, Cai L, Jiang C-y, Feng Y, Liu Z, Zeng Q, Cheng L, Sun YE. 2013. Genetic programs in human and mouse early embryos revealed by single-cell RNA sequencing. *Nature* **500**: 593-597.

Yan L, Yang M, Guo H, Yang L, Wu J, Li R, Liu P, Lian Y, Zheng X, Yan J et al. 2013. Single-cell RNA-Seq profiling of human preimplantation embryos and embryonic stem cells. *Nat Struct Mol Biol* **20**: 1131-1139.

Zappia L, Phipson B, Oshlack A. 2017. Splatter: simulation of single-cell RNA sequencing data. *Genome Biol* **18**: 174.

Zeisel A, Muñoz-Manchado AB, Codeluppi S, Lönnerberg P, La Manno G, Juréus A, Marques S, Munguba H, He L, Betsholtz C. 2015. Cell types in the mouse cortex and hippocampus revealed by single-cell RNA-seq. *Science* **347**: 1138-1142.

Zhang L, Yu X, Zheng L, Zhang Y, Li Y, Fang Q, Gao R, Kang B, Zhang Q, Huang JY. 2018. Lineage tracking reveals dynamic relationships of T cells in colorectal cancer. *Nature* **564**: 268.

Zhang P, Yang M, Zhang Y, Xiao S, Lai X, Tan A, Du S, Li S. 2019. Dissecting the Single-Cell Transcriptome Network Underlying Gastric Premalignant Lesions and Early Gastric Cancer. *Cell reports* **27**: 1934-1947. e1935.

Zheng C, Zheng L, Yoo J-K, Guo H, Zhang Y, Guo X, Kang B, Hu R, Huang JY, Zhang Q. 2017. Landscape of infiltrating T cells in liver cancer revealed by single-cell sequencing. *Cell* **169**: 1342-1356. e1316.